Journal Name

ARTICLE

Side-chain engineering in a thermal precursor approach for efficient photocurrent generation with insoluble tetrabenzoporphyrin–diketopyrrolopyrrole conjugates

Received 00th January 20xx,
Accepted 00th January 20xx

DOI: 10.1039/x0xx00000x

www.rsc.org/

Kohtaro Takahashi,[a] Daichi Kumagai,[b] Naoya Yamada,[b] Daiki Kuzuhara,[a] Yuji Yamaguchi,[b] Naoki Aratani,[a] Tomoyuki Koganezawa,[c] Sota Koshika,[d] Noriyuki Yoshimoto,[d] Sadahiro Masuo,[e] Mitsuharu Suzuki,*[a] Ken-ichi Nakayama,*[bf] and Hiroko Yamada*[a]

An ideal active-layer compound for bulk-heterojunction (BHJ) organic photovoltaic devices (OPVs) can assemble upon deposition to form the effective π–π stacking that facilitates exciton diffusion and charge-carrier transport. It is also expected to possess a high-enough miscibility for forming sufficient heterojunction to ensure efficient charge separation. However, these characteristics are often not compatible in organic small-molecule semiconductors: Compounds endowed with rich self π–π interaction capacity tend to be poor in miscibility, or may be even insoluble in extreme cases. Herein, we postulate that a thermal precursor approach can serve as a way out of this dilemma, provided that molecules are properly engineered. This work evaluates a series of diketopyrrolopyrrole (DPP)–tetrabenzoporphyrin (BP) conjugates named C*n*-DPP–BP (*n* = 4, 6, 8 or 10 depending on the length of alkyl groups on the DPP unit) as p-type material in BHJ OPVs. These compounds are strongly aggregating and insoluble, thus processed via the thermal precursor approach in which the corresponding soluble derivatives (C*n*-DPP–CP) are solution-processed into thin films and then converted to the target materials by in situ thermal reactions. The comparative study shows that the short-circuit current density largely depends on the length of alkyl substituents, ranging from 0.88 mA cm^{-2} with C10-DPP–BP to 15.2 mA cm^{-2} with C4-DPP–BP. Investigation into the structure of active layers through fluorescence-decay analysis, atomic-force microscopy, and two-dimensional grazing-incidence wide-angle X-ray diffractometry indicates that the introduction of shorter alkyl chains positively affects the miscibility and molecular orientation in BHJ layers. This trend is not fully parallel to those observed in the BHJ systems prepared through conventional solution techniques, and will provide a unique basis for devising a new class of high-performance OPV materials.

1. Introduction

The photon-to-electron conversion process in organic photovoltaic devices (OPVs) is accomplished by synergetic actions of multiple materials.[1] The design of OPV materials is therefore multilateral, requiring careful consideration to the balance among various aspects of the overall photovoltaic process. For instance, strong π–π interaction is favourable in terms of facilitating exciton diffusion and charge-carrier transport, while it may also lead to excessive aggregation and phase separation which limit charge separation by reducing the heterojunction.[2–6] Accordingly, the compromise between efficient self-interaction and sufficient miscibility is often a critical factor in designing active-layer materials for OPVs.

On the other hand, precursor approaches provide unique opportunities in the engineering of small-molecule OPV materials.[7–15] In the preparation of small-molecule thin films by precursor approaches, soluble precursor compounds are solution-processed into the thin-film form and then converted to target materials by quantitative in situ chemical reactions. A typical example is the preparation of tetrabenzoporphyrin (BP) thin films. BP is an insoluble p-type semiconductor, while its thermal precursor 1,4:8,11:15,18:22,25-tetraethano-29H,31H-tetrabenzo[b,g,l,q]porphyrin (CP) is well soluble. Thus, thin films of BP can be prepared in a stepwise manner where CP is solution-deposited then thermally converted to BP.[16–24] By taking advantage of such precursor approaches, it is possible to obtain well-performing small-molecule photovoltaic layers comprising highly crystalline, aggregating molecular semiconductors without sacrificing their intermolecular contacts. Matsuo et al. indeed employed the CP-to-BP conversion in the 2009 paper for preparing p–i–n-type organic photovoltaic layers having highly ordered crystalline nanophases that afforded a power-conversion efficiency (PCE) of 5.2%.[20] This was achieved by employing a specially designed n-type material named SIMEF, as well as carefully optimized

[a] Graduate School of Materials Science, Nara Institute of Science and Technology (NASIT), Ikoma, Japan. Email: hyamada@ms.naist.jp
[b] Department of Organic Device Engineering, Yamagata University, Yonezawa, Japan.
[c] Japan Synchrotron Radiation Research Institute (JASRI), SPring-8, Sayo, Japan.
[d] Graduate School of Engineering, Iwate University, Morioka, Japan
[e] Department of Applied Chemistry for Environment, Kwansei Gakuin University, Sanda, Japan.
[f] Department of Material and Life Science, Osaka University, Suita, Japan.

†Electronic Supplementary Information (ESI) available: Supplementary figures and tables, experimental details, UV–vis absorption spectra and ^{1}H and ^{13}C NMR spectra. CCDC for the crystal structure of C6-DPP–BP is 1491998. For ESI and crystallographic data in CIF format see DOI: 10.1039/x0xx00000x

thermal-annealing conditions and cathode buffer material. Notably, the 5.2% PCE was among the best achieved in small-molecule OPVs at that time, and still remains one of the highest reported for the OPVs having BP or its derivative in the active layer.

Meanwhile, the current state-of-the-art devices have achieved PCEs of over 10%,[4,25–30] and many research groups are working toward even higher efficiencies in order for realizing practical applications of OPVs. Along these lines, we have envisioned that a high-performance OPVs may be obtained by further exploiting the superior traits of BP (e.g., high absorption coefficient,[31] good hole transport capability,[32,33] and exceptional stability[34,35]) in combination with the use of thermal precursor approach for active-layer deposition.

A key task in this context is the enhancement of photocurrent-generation efficiency. BP has strong but rather narrow absorption bands, being transparent around 500–600 nm and over 700 nm.[20,36] In consequence of this limited photoabsorption window, short-circuit current density (J_{SC}) values of BP-based OPVs have been relatively low; for instance, the p–i–n system reported by Matsuo et al. showed a J_{SC} of 10.5 mA cm^{-2} at maximum,[20] while the current-best cells typically afford J_{SC}s of 15–20 mA cm^{-2}.[4,25–30] Thus, expansion of the absorption range is a primary factor in designing π-conjugated frameworks of BP-based photoabsorbers. Another important factor in improving J_{SC} is the substituent effect. It is well known that the photovoltaic performance of organic semiconductors largely depend not only on the structure of main π-framework, but also on the structure and position of peripheral substituents. For instance, Shin et al. reported that the structural difference of alkyl chains on a diketopyrrolopyrrole (DPP)-based small-molecule system brought about a considerable variation in J_{SC} ranging from below 4 to over 8 mA cm^{-2} and accordingly in PCE from 1.1 to 4.2%.[37] This and many other examples have demonstrated the strong impact of substituents on the charge-carrier generation and transport efficiencies in organic photovoltaic layers.[37–40]

With these in mind, we have designed a series of DPP–BP conjugates that can efficiently absorb at a wide range of wavelengths in the visible and near-infrared region. These conjugates have linear alkyl chains on the DPP units, and are denoted as C*n*-DPP–BP in which *n* is either 2, 4, 6, 8, or 10 depending on the length of alkyl chains. C*n*-DPP–BPs are all insoluble in common organic solvents, and thus solution-deposited via the thermal precursor approach from the corresponding CP derivatives (Scheme 1).

The following sections compare bulk-heterojunction (BHJ) OPVs comprising C*n*-DPP–BP and [6,6]-phenyl-C_{61}-buthylic acid methyl ester ($PC_{61}BM$), and reveal that the length of alkyl chains greatly affects the performance of the resulting devices. The J_{SC} ranges from 0.88 mA cm^{-2} with C10-DPP–BP to 15.2 mA cm^{-2} with C4-DPP–BP, resulting in PCEs of 0.19 and 5.2%, respectively. The origin of this large substituent impact is discussed based on analyses of the active layers by fluorescence decay measurements, atomic-force microscopy (AFM), and two-dimensional grazing-incidence wide-angle X-ray diffractometry (2D-GIWAXD). It is shown that the introduction of shorter alkyl chains suppresses the propensity of C*n*-DPP–BP molecules to form large aggregates and to adopt edge-on-mode geometry, which positively affects the photocurrent-generation efficiency in BHJ films. These results would provide a basis of molecular design in the thermal precursor approach toward preparing photovoltaic active layers with ideal morphology.

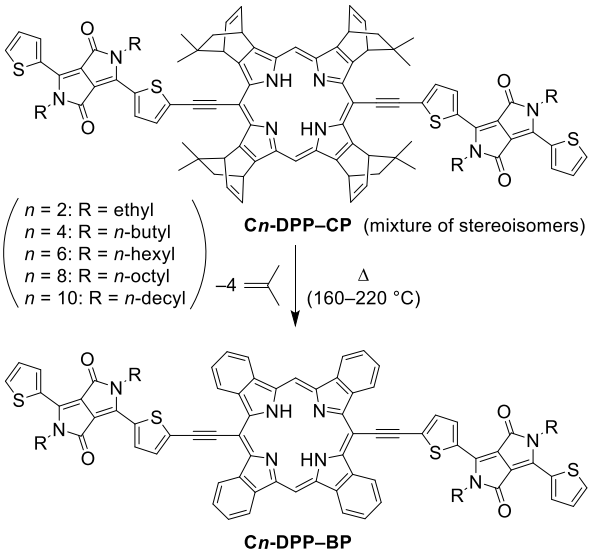

Scheme 1 Formation of C*n*-DPP–BPs from the corresponding thermal precursors C*n*-DPP–CPs.

2. Results and discussion

2.1. Molecular design and synthesis

C*n*-DPP–BPs have an acceptor–donor–acceptor (A–D–A) structure in which BP and DPP serve as donor and acceptor units, respectively. The A–D–A configuration has been a widely employed molecular design to achieve desirable frontier-orbital energy levels and effective π-conjugation in state-of-the-art active-layer compounds for OPVs.[41] The DPP chromophore is chosen as a partner of BP, because DPP strongly absorbs around 550 nm at which BP's absorption valley locates.[42] The BP and DPP units are connected through the sterically non-demanding ethynylene linkage in order to minimize the steric hindrance between the benzo moieties and the *meso* substituents of BP. The geometry optimization by density functional theory (DFT) has predicted that C*n*-DPP–BPs possess relatively planar molecular conformations associated with efficient π-conjugation (Fig. S1, ESI†). A related molecular design has been employed for soluble small-molecule photoabsorbers based on the non-benzoannulated zinc porphyrin chromophore.[43,44]

The peripheral substituents of C*n*-DPP–BPs are kept minimal; namely, each molecule is equipped with only four linear, relatively short alkyl chains at the nitrogen atoms of DPP moieties. Accordingly, C*n*-DPP–BPs are all insoluble in common organic solvents. This molecular design is made possible by employing the precursor approach and beneficial in that such large π-systems as C*n*-DPP–BPs do not require the heavy decoration with insulating solubilizing groups that are unnecessary in terms of the optimization of thin-film

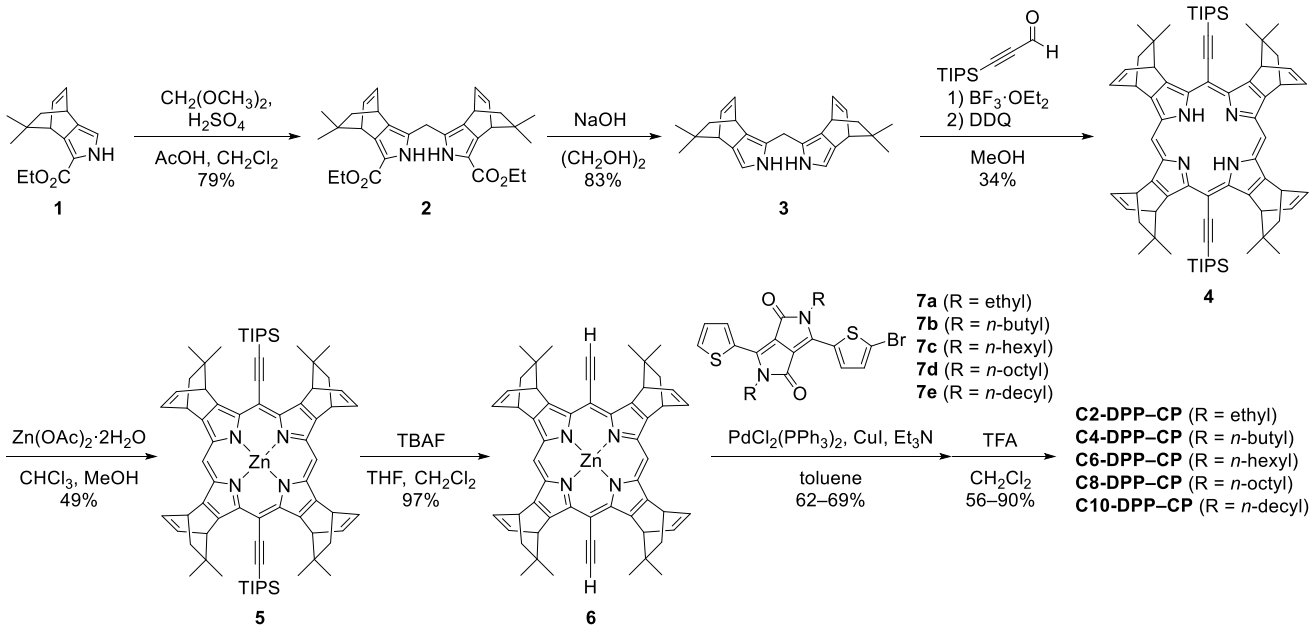

Scheme 2 Synthesis of C*n*-DPP–CPs. Starting material **1** and all the products were isolated and used as mixtures of stereoisomers.

morphology and molecular packing.

The corresponding precursors C*n*-DPP–CPs have four dimethylethano bridges as thermally removable solubilizing units in order for ensuring the enough solubility for synthesis and solution deposition.[16,45,46] Note that the original CP has four non-methylated ethano bridges which are often insufficient for solubilizing π-extended BP derivatives.

The synthesis of C*n*-DPP–CPs is summarized in Scheme 2. Pyrrole **1** was prepared according to the literature,[46] which was then subjected to the double condensation with dimethoxymethane and hydrolytic decarboxylation to form dipyrromethane **3**. The "2 + 2"-type MacDonald condensation of **3** with 3-triisopropylsilyl-2-propynal in the presence of $BF_3{\cdot}OEt_2$[47,48] followed by the oxidation with 2,3-dichloro-5,6-dicyano-1,4-benzoquinone (DDQ) afforded porphyrin **4** in 34% yield. Here, while five diastereomers are possible to form depending on the relative orientation of four dimethylethano bridges against the porphyrin plane, a mixture of only two diastereomers was used in the following step (see the synthetic procedure, ESI†). After insertion of a zinc(II) ion, the triisopyropylsilyl (TIPS) groups were removed by the action of tetrabutylammonium fluoride (TBAF) to afford porphyrin **6**. The target thermal precursors C*n*-DPP–CPs were obtained by the Sonogashira coupling of zinc porphyrin **6** with brominated DPP derivatives **7a**–**7e**,[49] and the dezincification with trifluoroacetic acid.

The proper connectivity among the CP, DPP, and ethynylene units was confirmed by single-crystal X-ray diffraction analysis of C6-DPP–CP (Fig. S2 and Table S1, ESI†). The torsion angles between the porphyrin and DPP planes in the crystal structure are 10° and 17°. Similar planarity can be expected for C*n*-DPP–BPs after the thermal conversion, because the steric hindrance between the central porphyrin core and side units should not be much different before and after the extrusion of isobutylene units. Thermogravimetric traces of C*n*-DPP–CPs show that the thermally induced retro-Diels–Alder reactions to C*n*-DPP–BPs start around 130–140 °C (Fig. S3, ESI†)

2.2. Optical and electronic properties

The optical absorption spectra of thin films of BP and C*n*-DPP–BP are compared in Fig. 1. BP shows strong absorptions around 400 and 700 nm corresponding to the Soret and Q bands, respectively, while the absorption between these bands are weak and the absorption extends to merely about 720 nm. On the other hand, C*n*-DPP–BPs generally show broader absorption than BP with absorption edge wavelengths reaching well beyond 800 nm. The locations of absorption edges are slightly different among C*n*-DPP–BPs, indicating that there are minor differences in solid-state molecular arrangement depending on the length of alkyl chains.

The highest occupied molecular orbital (HOMO) levels of C*n*-DPP–BPs were determined by photoelectron spectrometry as –5.0 or –5.1 eV (Fig. S4, ESI†). The optical energy gap (E_g) values were calculated from the absorption onsets of thin films as 1.44–1.47 eV, and the lowest unoccupied molecular orbital (LUMO) levels were calculated from these values to be –3.5 to –3.7 eV. As summarized in Table 1, the HOMO and LUMO levels of C*n*-DPP–BPs are lower than those of BP in the thin-film state by 0.1–0.2 and 0.3–0.5 eV, respectively.[50] Considering the general relationship between the open-circuit voltage (V_{OC}) and the HOMO level of donor, the V_{OC}s of C*n*-DPP–BP:$PC_{61}BM$ systems are expected to be higher than that of BP:$PC_{61}BM$.

2.3. Photovoltaic performance

BHJ OPVs with a general device structure of [ITO/PEDOT:PSS/ C*n*-DPP–BP:$PC_{61}BM$/Ca/Al] were fabricated via the thermal

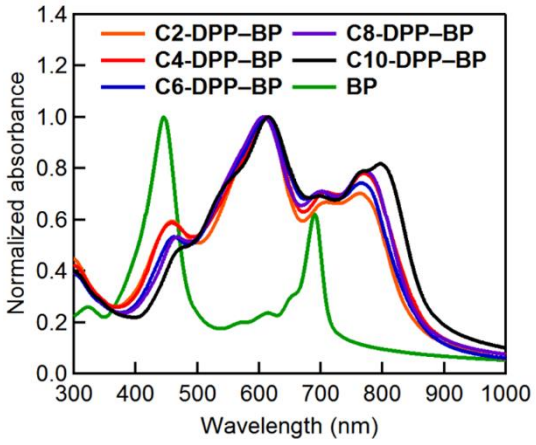

Fig. 1 Absorption spectra of BP and C*n*-DPP–BP thin films.

Table 1 Optical and electronic properties of C*n*-DPP–BPs and BP.

Materials[a]	λ_{onset} (nm)	E_g (eV)[b]	HOMO (eV)[c]	LUMO (eV)[d]
C2-DPP–BP	846	1.47	–5.0	–3.5
C4-DPP–BP	862	1.44	–5.0	–3.6
C6-DPP–BP	857	1.45	–5.0	–3.6
C8-DPP–BP	855	1.45	–5.0	–3.5
C10-DPP–BP	868	1.43	–5.1	–3.7
BP	716	1.73	–4.9	–3.2

[a]As thin films. [b]Calculated from λ_{onset}. [c]Determined by photoelectron spectroscopy in air. [d]Calculated as HOMO + E_g.

precursor approach using C*n*-DPP–CPs as precursors of C*n*-DPP–BPs. The relative amount against $PC_{61}BM$, thermal conversion conditions, and concentration of cast solution were optimized for each C*n*-DPP–BP (Tables S2–S13, ESI†). Unfortunately, thin films containing C2-DPP–BP were found too rough to be evaluated for OPV performance (Fig. S5, ESI†); thus, C2-DPP–BP was not studied further.

The current-density–voltage (*J*–*V*) curves and external quantum efficiency (EQE) spectra of the best-performing cells are plotted in Fig. 2a,b, and the obtained photovoltaic parameters are summarized in Table 2. The best result was obtained with C4-DPP–BP affording the maximum PCE of 5.2% (J_{SC} = 15.2 mA cm^{-2}, V_{OC} = 0.67 V, FF (fill factor) = 0.52). This efficiency is much higher than those obtained in BP:$PC_{61}BM$ and BP:PCBNB (≤0.1%, PCBNB: [6,6]-phenyl-C_{61}-butyric acid *n*-butyl ether).[5,50] Moreover, the 5.2% PCE is close to the best efficiencies reported so far for BP-based OPVs (5.2–5.4%) that have been achieved by using the specially designed n-type materials SIMEF[20] and (*o*-anisylsilylmethyl)(phenyl-silylmethyl)[60]fullerene (SIMEF-Ph, *o*-An)[51] in optimized p–i–n-type active layers.

Notably, the J_{SC} of 15.2 mA cm^{-2} obtained in the C4-DPP–BP:$PC_{61}BM$ system is considerably higher than those in the BP:$PC_{61}BM$ (5.7–7.0 mA cm^{-2})[20,32] and BP:SIMEF systems (10.2–10.5 mA cm^{-2}).[20,51] The EQE spectrum shows that the photovoltaic response of the C4-DPP–BP:$PC_{61}BM$ device well exceeds 700 nm and reaches 850 nm where pristine BP does not absorb (Fig. 2b). This is apparently owing to the extended π-conjugation with two DPP units, serving as a major contributing

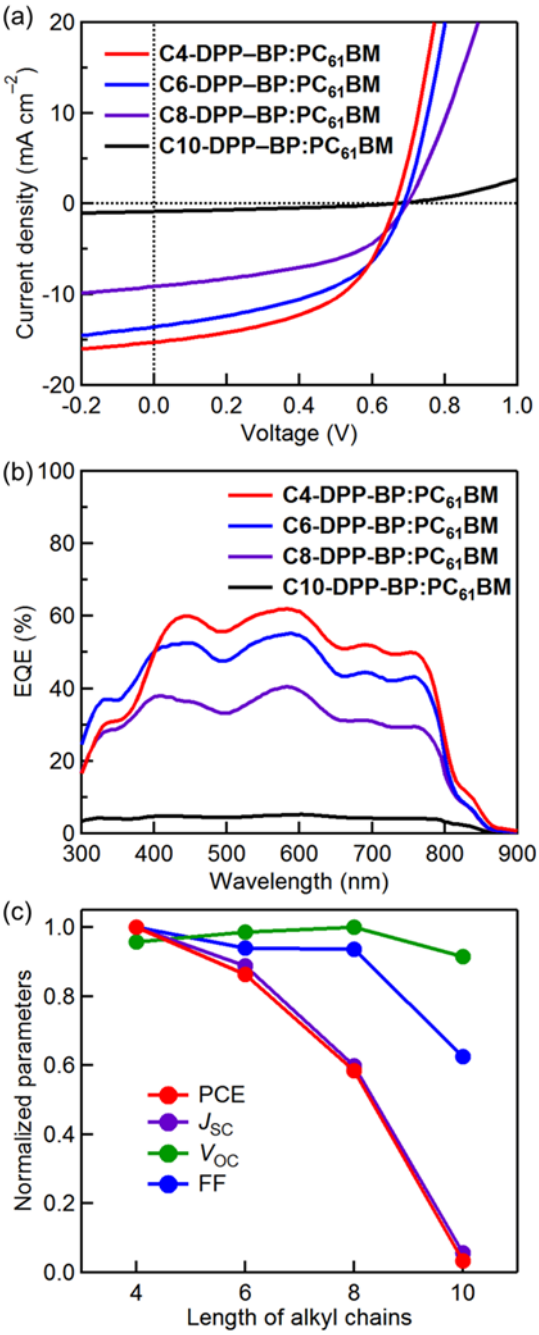

Fig. 2 (a) *J*–*V* curves, (b) EQE spectra, and (c) normalized photovoltaic parameters of the best-performing BHJ cells. Measurements were performed under AM 1.5G illumination at 100 mW cm^{-2}.

factor to the high J_{SC}. The V_{OC} of 0.67 V in the C4-DPP–BP:$PC_{61}BM$ system is slightly increased from those in BP:$PC_{61}BM$ devices (0.44–0.61 V), [32,52] reflecting the lower HOMO level of C4-DPP–BP (–5.0 eV) than that of BP (–4.9 eV). In addition, the FF of 0.52 is significantly improved from that of a BP:$PC_{61}BM$ BHJ device (0.23),[5] which is probably because of the superior morphology in the present case of C4-DPP–BP as compared to pristine BP (see Section 2.4). At the same time, however, the 0.52 FF is still lower as compared to those in the state-of-the-art cells which typically afford FFs around 0.7.[4,25–30] It has been reported that the FF can be improved by employing the p–i–n

Table 2 Photovoltaic parameters of optimized C*n*-DPP–BP:$PC_{61}BM$ OPVs and hole mobilities in blend films.[a]

p-Type material	Thickness (nm)[b]	J_{SC} (mA cm^{-2})[c]	V_{OC} (V)[c]	FF[c]	PCE (%)[c]	PCE_{ave} (%)[d]	μ_h (cm^2 V^{-1} s^{-1})
C4-DPP–BP	105	15.2	0.67	0.52	5.2	5.0 ± 0.1	2.2×10^{-4}
C6-DPP–BP	115	13.6	0.69	0.49	4.5	4.4 ± 0.1	1.7×10^{-4}
C8-DPP–BP	115	9.1	0.70	0.48	3.1	3.0 ± 0.1	1.5×10^{-4}
C10-DPP–BP	115	0.88	0.66	0.33	0.19	0.18 ± 0.01	0.60×10^{-4}

[a]Obtained under AM1.5G illumination at 100 mW cm^{-2}. [b]Active-layer thickness. [c]Parameters of the best-performing cells. [d]Averages and standard deviations of four devices.

configuration rather than BHJ as active-layer structure,[14,50,52] which may also be the case with C4-DPP–BP. This aspect is beyond the scope of the present work of obtaining well-performing BHJ layer, and will be examined elsewhere.

Fig. 2c shows plots of normalized OPV parameters against the length of alkyl chains. The PCE decreases together with the J_{SC} as alkyl chains become longer from C4- to C10-DPP–BP, while the V_{OC} is essentially unchanged among all the four derivatives. The FF is constant around 0.5 with the C4-, C6-, and C8-derivatives, but considerably decreases to 0.33 in the case of C10-DPP–BP. In order to understand the observed dependence on the alkyl-chain length, the charge-transfer efficiency, charge-carrier mobility, and charge-recombination efficiency of each blend film were examined.

The charge-transfer efficiency was evaluated using a picosecond-pulsed laser excitation at 470 nm followed by the measurement of the average fluorescence lifetime (τ_f) in each BHJ layer (Fig. 3a). The obtained τ_f values are smaller with shorter alkyl chains; namely, 0.45 ns for C4-DPP–BP:$PC_{61}BM$, 0.48 ns for C6-DPP–BP:$PC_{61}BM$, 0.54 ns for C8-DPP–BP:$PC_{61}BM$, and 0.70 ns for C10-DPP–BP:$PC_{61}BM$. This result suggests that more effective fluorescence quenching via charge separation occurs with shorter alkyl chains.[16,36] In other words, C*n*-DPP–BPs are more finely mixed with $PC_{61}BM$ when the alkyl substituents on the DPP units are shorter.

Next, the hole mobility (μ_h) in each blend film was measured by the space-charge-limited current (SCLC) method in hole-only devices with a general structure of [ITO/PEDOT:PSS/C*n*-DPP–BP:$PC_{61}BM$/MoO_3/Al] (Table 2, and Fig. S6, ESI†). The organic layers were deposited under the same conditions as those optimized for BHJ OPVs. The measurements have revealed that the μ_h increases from 0.60 to 2.2 × 10^{-4} cm^2 V^{-1} s^{-1} as the alkyl substituents become shorter form C10 to C4. Thus, the C4-DPP–BP:$PC_{61}BM$ blend is the best in terms of the efficiency of hole transport toward the anode among the examined systems. Improvement in μ_h generally leads to higher J_{SC} and FF values,[29,44,53] which is also the case for C*n*-DPP–BP:$PC_{61}BM$.

We then measured the variation in J_{SC} as a function of illumination intensity to evaluate the charge-recombination characteristics (Fig. 3b).[54,55] In general, the power-law dependence of J_{SC} upon light intensity is observed for OPVs; namely, $J_{SC} \propto I^{\alpha}$ where α is an exponential factor, and $\alpha = 1$ indicates the efficient sweep out of carriers prior to recombination. The α values are high for the C4-, C6-, and C8-DPP–BP:$PC_{61}BM$ devices, being 1, 1, and 0.98, respectively. On the other hand, the C10-DPP–BP:$PC_{61}BM$ device showed an α of 0.88, suggesting that the bimolecular charge recombination is promoted in this case compared to other systems with shorter alkyl chains. Thus, the non-geminate charge recombination is suppressed when alkyl groups are shorter.

2.4. Surface morphology

The surface morphology of C*n*-DPP–BP:$PC_{61}BM$ films probed by AFM are shown in Fig. 4a–d. Pinholes, which lower the performance and stability of OPVs,[56,57] are noticeable in all the cases, although their depth and appearance frequency are largely dependent on the length of alkyl substituents. The depth of the deepest pinhole in each probed area is about 10, 12, 37, and 34 nm for the C4-, C6-, C8-, and C10-DPP–BP blend films, respectively (Fig. S7, ESI†). Pinholes or cracks are noticeable also in neat films of C*n*-DPP–BPs (Fig. S8, ESI†) and other previously reported BP derivatives deposited by the thermal

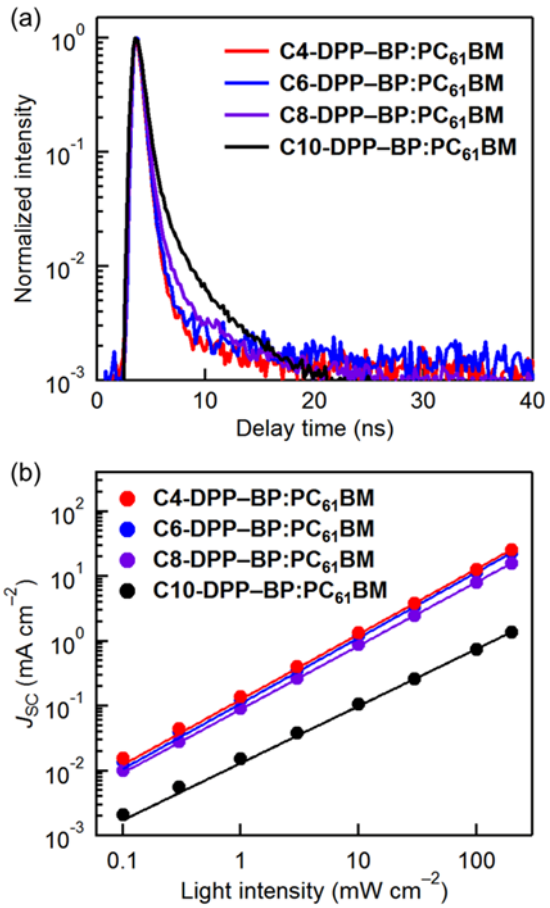

Fig. 3 (a) Fluorescence lifetime decay curves and (b) light-intensity dependency of J_{SC} for the optimized BHJ OPVs.

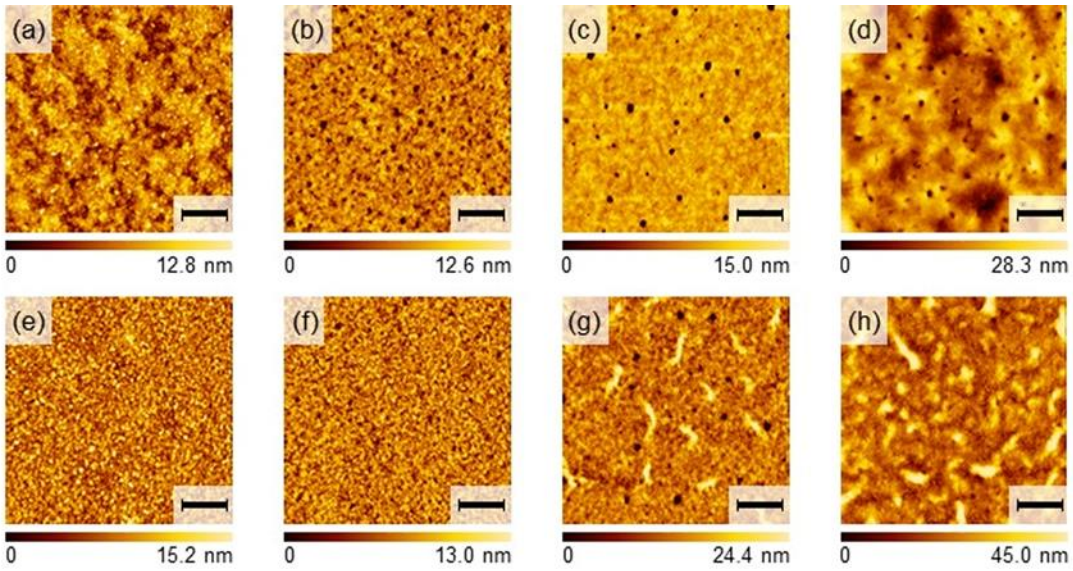

Fig. 4 Tapping-mode AFM images. (a) C4-DPP–BP:$PC_{61}BM$, (b) C6-DPP–BP:$PC_{61}BM$, (c) C8-DPP–BP:$PC_{61}BM$, (d) C10-DPP–BP:$PC_{61}BM$, (e) rinsed C4-DPP–BP:$PC_{61}BM$, (f) rinsed C6-DPP–BP:$PC_{61}BM$, (g) rinsed C8-DPP–BP:$PC_{61}BM$, and (h) rinsed C10-DPP–BP:$PC_{61}BM$. The scale bars correspond to 1 μm.

precursor approach.[15] In all these cases, such morphological defects become more prominent when larger alkyl groups were introduced as substituents. These observations suggest that the formation of large structural defects in thin films would be facilitated as molecules become more mobile and easier to rearrange during the thermal conversion process.

We also observed the surface morphology of blend films after rinsing with toluene. Since C*n*-DPP–BPs are insoluble in toluene (Fig. S9, ESI†), it is possible to wash away $PC_{61}BM$ from the blend films and directly observe the morphology of remaining C*n*-DPP–BP domains (Fig. 4e–h).[20,32] Micrometer-sized grains exist in the cases of C8- and C10-DPP–BP, whereas grains are around 100 nm or smaller in the cases of C4- and C6-DPP–BP. These results are in accordance with the above postulation that longer alkyl chains would bring about higher molecular mobility during the thermal conversion process, resulting in more significant self-aggregation and formation of larger domains. Considering that typical exciton diffusion lengths in molecular organic materials are within the range of only a few to tens of nanometers,[58] the grains in C8- and C10-DPP–BP:$PC_{61}BM$ films are too large to allow efficient charge separation.

2.5. Molecular orientation and crystallinity

The molecular arrangement in C*n*-DPP–BP neat films and C*n*-DPP–BP:$PC_{61}BP$ blend films were analysed by 2D-GIWAXD measurements.[59] Fig. 6a–h and 6i,j show the 2D-GIWAXD images and their out-of-plane profiles, respectively (see Fig. S10, S11 and Tables S14, S15, ESI† for the exact peak positions and the corresponding *d*-spacing values).

The C4- and C6-DPP–BP neat films show combinations of a low-wavenumber diffraction in the in-plane direction (q_{xy} = 0.48 $Å^{-1}$, *d* = 13 Å) and a high-wavenumber diffraction in the out-of-plane direction (q_z = 1.79 $Å^{-1}$, *d* = 3.5 Å). The former diffraction roughly corresponds to the edge-to-edge dimension of the BP framework (Fig. S12, ESI†), and the latter to the π–π stacking distance. Thus, these pairs of diffraction peaks indicate that molecules of C4- and C6-DPP–BP are arranged in face-on geometries in neat films, which is favourable for the out-of-plane carrier transport in OPVs.[28] The C8-DPP–BP neat film shows arc-shaped diffraction patterns at around q = 0.35 $Å^{-1}$ (*d* = 18 Å) and 1.75 $Å^{-1}$ (3.6 Å) indicating random arrangement of crystallites.[60] A combination of a primary peak in the out- of-plane direction (q_z = 0.33 $Å^{-1}$, *d* = 19 Å) and a peak from the π–π stacking in the in-plane direction (q_{xy} = 1.74 $Å^{-1}$, *d*= 3.6 Å) is apparent in the data of C10-DPP–BP neat film, suggesting that C10-DPP–BP molecules stack mainly in the edge-on mode. The C10-DPP–BP neat film also shows higher-order peaks in the out-of-plane direction (q_z = 0.65 and 0.94 $Å^{-1}$) indicating a higher crystallinity as compared to the other neat films.

It is noteworthy that the molecular orientation in C*n*-DPP–BP neat films drastically changes only by altering the alkyl-chain length. Although the origin of this result is not clear at this moment, one possible factor is the aspect ratio of molecules. The aspect ratio of C*n*-DPP–BP molecules with extended alkyl chains increases from C10-DPP–BP to C4-DPP–BP (Fig. S13, ESI†), and the molecular orientation changes from edge-on to face-on as the ratio increases. Similar trends have been reported with solution-processable small-molecules by Cheng et al.[29,61] and Bazan et al.[62,63] In these reports, the molecular orientation in neat films changes from edge-on to face-on upon increasing the longer axis of molecules and thus the aspect ratio (Fig. S14 and S15, ESI†).

On the other hand, the edge-on orientation was found to be a preferred molecular arrangement regardless of the alkyl-chain length in the blend films (Fig. 5e–h). The diffraction pattern of the C10-DPP–BP:$PC_{61}BM$ film is very similar to that of the C10-DPP–BP neat film, demonstrating that C10-DPP–BP molecules

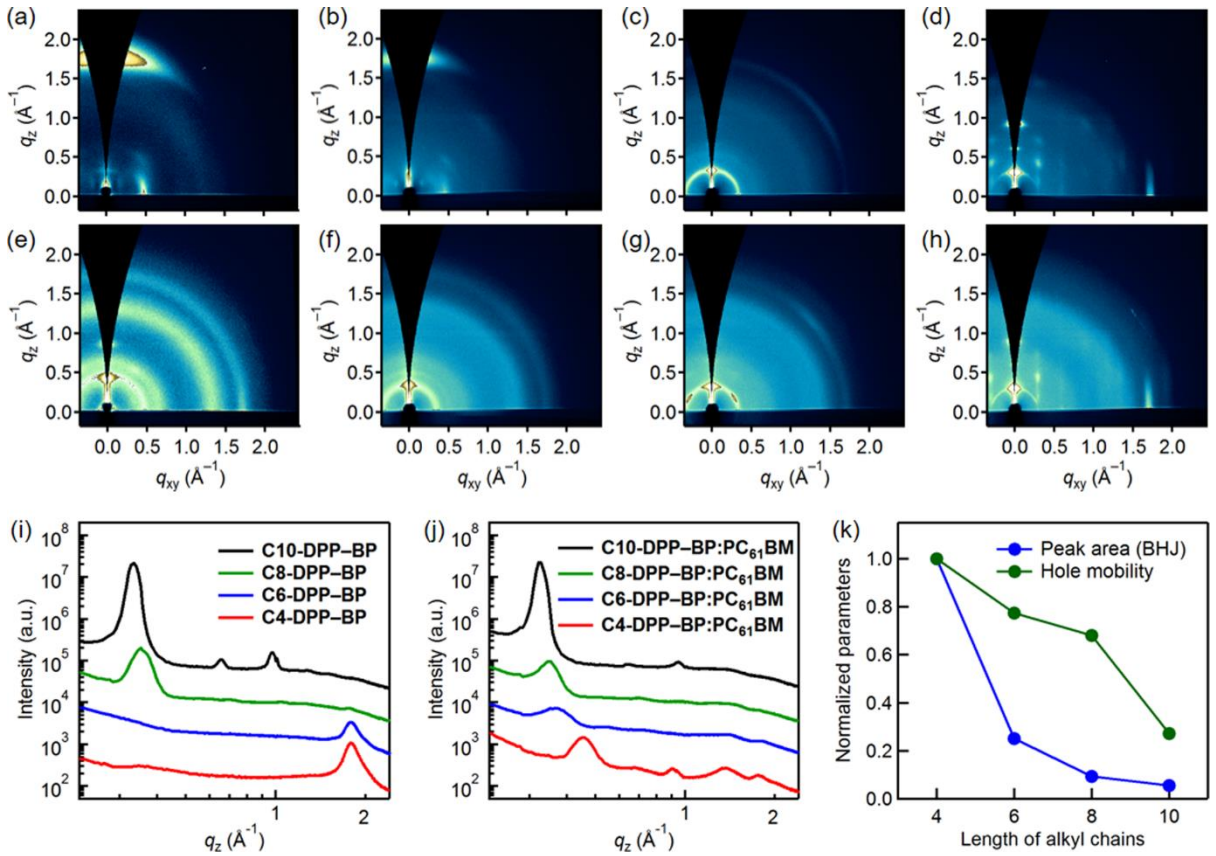

Fig. 5 2D-GIWAXD images of (a) C4-DPP–BP, (b) C6-DPP–BP, (c) C8-DPP–BP, (d) C10-DPP–BP, (e) C4-DPP–BP:PC$_{61}$BM, (f) C6-DPP–BP:PC$_{61}$BM, (g) C8-DPP–BP:PC$_{61}$BM, (h) C10-DPP–BP:PC$_{61}$BM; out-of-plane profiles of 2D-GIWAXD images of (i) the C*n*-DPP–BP neat films and (j) the C*n*-DPP–BP:PC$_{61}$BM blend films; and (k) correlation of peak areas in out-of-plane profiles and hole mobilities in blend films with the alkyl-chain length.

take the edge-on geometry with high selectivity in the blend film as well (Fig. 5h, Fig. S10d and S11d, ESI†). Thus, the out-of-plane carrier transport should be inefficient in the C10-DPP–BP:PC$_{61}$BM blend, which is reflected to the low J_{SC} and FF in the corresponding OPVs.[64] In the case of C8-DPP–BP:PC$_{61}$BM, a relatively strong π–π stacking peak (q = 1.74 Å^{-1}, d = 3.61 Å) is observed at 20–60° from the q_{xy} axis, indicating that the effective charge-carrier paths based on C8-DPP–BP molecules point diagonally to the substrates (Fig. S16, ESI†). This orientation is less favourable for the charge extraction in OPVs than the exact face-on orientation but would be better than the edge-on orientation. The π–π stacking diffraction from the C6-DPP–BP:PC$_{61}$BM film is arc-shaped; thus the charge-carrier transport via C6-DPP–BP molecules does not have preferred orientation in this blend film. This type of molecular arrangement is often observed in efficient small-molecule BHJ OPVs.[29,43] The diffraction pattern of the C4-DPP–BP:PC$_{61}$BM film is similar to that of the C6-DPP–BP:PC$_{61}$BM film, while the diffraction intensity is higher for the former. The observed molecular arrangements in the blend films seem more or less reflecting those of C*n*-DPP–BP neat films in which a derivative with shorter alkyl chains shows a stronger tendency to adopt the face-on geometry.

We then calculated the peak areas corresponding to the π–π stacking of C*n*-DPP–BP molecules in the out-of-plane direction in order to compare the populations of effective charge-carrier paths among the C*n*-DPP–BP:PC$_{61}$BM films. Note that the peak area serves as a relative measure of the crystallite volume within thin films.[65] The values were obtained by applying the Gaussian fitting to the out-of-plane profiles of 2D-GIWAXD images (Fig. S17, ESI†),[66] and found to increase as the alkyl-chain length decrease. The SCLC hole mobility roughly follows this trend (Fig. 5k), well demonstrating the positive impact of face-on stacking on the charge-carrier transport and thus J_{SC} and FF in OPVs.

3. Conclusions

This study has explored the side-chain effect on the photovoltaic performance of a series of small-molecule BHJ thin films prepared via the thermal precursor approach. The systematic evaluation of C*n*-DPP–BP:PC$_{61}$BM systems showed that the length of alkyl chains on C*n*-DPP–BP molecules strongly influenced the efficiency of resulting OPVs; namely, the PCE improved from 0.19 to 5.2% as the alkyl chains became shorter from *n*-decyl (C10) to *n*-butyl (C4). A large part of this change could be ascribed to JSC that increased from 0.88 to 15.2 mA cm^{-2}. The analyses of thin film properties confirmed that the best-performing compound C4-DPP–BP was superior to the longer-alkyl-chain derivatives in terms of both the charge-carrier generation and transport efficiencies owing to the more

preferable morphology and π–π-stacking orientation in the BHJ layer. On the other hand, the worst-performing derivative C10-DPP–BP formed extremely large aggregates and adopted the edge-on geometry in high selectively, which would both adversely affect the charge-carrier generation and transport.

These observations with C*n*-DPP–BPs are not fully parallel to those with conventional solution-processable small molecules. For example, solution-processable small molecules for BHJ OPVs usually require extensive decollation with bulky, flexible substituents to ensure the solubility in deposition solvent and the miscibility with partner material. By contrast, in the present case of thermal precursor approach, the π-framework of DPP–BP conjugates requires as compact substituents as possible in order to form favourable morphology for the photovoltaic process. It is presumed that this result relates to the high tendency of C*n*-DPP–BP molecules to self-aggregate and their mobility during the thermal conversion from CP to BP at relatively high temperatures of ≥160 °C.

In addition, the dependency of molecular orientation on the substituent structure should not be exactly the same between the thermal precursor approach and other solution processes. This is because the molecular orientation in thin films is sensitive to many kinetic and thermodynamic factors which are considerably differing between deposition methods.[67–69] Nevertheless, the thermal precursor approach seems to have some aspects in common with other deposition processes, as exemplified with the aspect ratio–molecular orientation relationship mentioned in Section 2.5. Our capacity for controlling the morphology and molecular orientation in solution-processed small-molecule thin films will benefit from further study on the characteristics of the thermal precursor approach.

It would be worth noting here again that the thermal precursor approach provides unique opportunities in designing molecules and active layers for OPVs. In terms of the molecular design, the present method allows us to minimize solubilizing substituents that are insulating and often limit effective intermolecular π–π contacts. It also enables insolubilizing post-deposition films and thus constructing multilayer structures by repeating the solution deposition–thermal conversion cycle as demonstrated in the preparation of well-performing p–i–n system by Matsuo et al.[20] In fact, the C4-DPP–BP:$PC_{61}BM$ BHJ system has shown a rather low FF (0.55) associated with increasing current density at negative bias voltages; therefore, higher performance can be expected by employing the p–i–n architecture to improve the charge-extraction efficiency. Work along these lines is underway in our group.

Acknowledgements

This work was supported by CREST program of the Japan Science and Technology Agency (JST) (SM, KN, HY), Grants-in-Aid for Scientific Research (KAKENHI) (JP26105004 (HY), JP16K17949 (MS), JP26288038 (NA), JP26390023 (SM), and JP16H02286 (HY)) from the Japan Society for the Promotion of Science (JSPS), the program for promoting the enhancement of research universities in NAIST supported by the Ministry of Education, Culture, Sports, Science and Technology (MEXT), Grant-in-Aid for JSPS Research Fellow (JP16J04335, KT) and Foundation for NAIST (KT and MS). We acknowledge Nippon Synthetic Chem. Ind. (Osaka, Japan) for a gift of ethyl isocyanoacetate, which was used for the preparation of the starting pyrrole. We also thank R. Abe and Ms. Y. Nishikawa in NAIST for the analysis of 2D-GIWAXD images and mass spectroscopy, respectively. The synchrotron experiments were performed at beamlines BL19B2 and BL46XU in SPring-8 with the approval of the Japan Synchrotron Radiation Research Institute (JASRI) (Proposal No. 2015A1683 (MS), 2015A1842 (KT), 2015A1965 (TK), and 2015B1769 (KT)).

Notes and references

1 K. Leo, *Elementary Processes in Organic Photovoltaics*, Springer International Publishing, Switzerland, 2017.
2 K. L. Gu, Y. Zhou, X. Gu, H. Yan, Y. Diao, T. Kurosawa, B. Ganapathysubramanian, M. F. Toney and Z. Bao, *Org. Electron.*, 2017, **40**, 79–87.
3 O. K. Kwon, M. A. Uddin, J.-H. Park, S. K. Park, T. L. Nguyen, H. Y. Woo and S. Y. Park, *Adv. Mater.*, 2016, **28**, 910–916.
4 Y. Liu, J. Zhao, Z. Li, C. Mu, W. Ma, H. Hu, K. Jiang, H. Lin, H. Ade and H. Yan, *Nat. Commun.*, 2014, **5**, 5293.
5 Y. Tamura, H. Saeki, J. Hashizume, Y. Okazaki, D. Kuzuhara, M. Suzuki, N. Aratani and H. Yamada, *Chem. Commun.*, 2014, **50**, 10379–10381.
6 H. Najafov, B. Lee, Q. Zhou, L. C. Feldman and V. Podzorov, *Nat. Mater.*, 2010, **9**, 938–943.
7 T. Umeyama, D. Matano, S. Shibata, J. Baek, S. Ito and H. Imahori, *ECS J. Solid State Sci. Technol.*, 2017, **6**, M3078–M3083.
8 K. Kawajiri, T. Kawanoue, M. Yamato, K. Terai, M. Yamashita, M. Furukawa, N. Aratani, M. Suzuki, K. Nakayama and H. Yamada, *ECS J. Solid State Sci. Technol.*, 2017, **6**, M3068–M3074.
9 T. Umeyama, S. Shibata and H. Imahori, *RSC Adv.*, 2016, **6**, 83758–83766.
10 Y. Tamura, D. Kuzuhara, M. Suzuki, H. Hayashi, N. Aratani and H. Yamada, *J. Mater. Chem. A*, 2016, **4**, 15333–15342.
11 M. Suzuki, Y. Yamaguchi, K. Takahashi, K. Takahira, T. Koganezawa, S. Masuo, K. Nakayama and H. Yamada, *ACS Appl. Mater. Interfaces*, 2016, **8**, 8644–8651.
12 C. Quinton, M. Suzuki, Y. Kaneshige, Y. Tatenaka, C. Katagiri, Y. Yamaguchi, D. Kuzuhara, N. Aratani, K. Nakayama and H. Yamada, *J. Mater. Chem. C*, 2015, **3**, 5995–6005.
13 S. Masuo, W. Sato, Y. Yamaguchi, M. Suzuki, K. Nakayama and H. Yamada, *Photochem. Photobiol. Sci.*, 2015, **14**, 883–890.
14 Y. Yamaguchi, M. Suzuki, T. Motoyama, S. Sugii, C. Katagiri, K. Takahira, S. Ikeda, H. Yamada and K. Nakayama, *Sci. Rep.*, 2014, **4**, 7151.
15 K. Takahashi, N. Yamada, D. Kumagai, D. Kuzuhara, M. Suzuki, Y. Yamaguchi, N. Aratani, K. Nakayama and H. Yamada, *J. Porphyr. Phthalocyanines*, 2015, **19**, 465–478.
16 Y. Zhen, H. Tanaka, K. Harano, S. Okada, Y. Matsuo and E. Nakamura, *J. Am. Chem. Soc.*, 2015, **137**, 2247–2252.
17 C. D. Liman, S. Choi, D. W. Breiby, J. E. Cochran, M. F. Toney, E. J. Kramer and M. L. Chabinyc, *J. Phys. Chem. B*, 2013, **117**, 14557–14567.
18 P. B. Shea, H. Yamada, N. Ono and J. Kanicki, *Thin Solid Films*, 2012, **520**, 4031–4035.
19 N. Noguchi, S. Junwei, H. Asatani and M. Matsuoka, *Cryst. Growth Des.*, 2010, **10**, 1848–1853.
20 Y. Matsuo, Y. Sato, T. Niinomi, I. Soga, H. Tanaka and E. Nakamura, *J. Am. Chem. Soc.*, 2009, **131**, 16048–16050.

21 P. B. Shea, L. R. Pattison, M. Kawano, C. Chen, J. Chen, P. Petroff, D. C. Martin, H. Yamada, N. Ono and J. Kanicki, *Synth. Met.*, 2007, **157**, 190–197.
22 P. B. Shea, J. Kanicki, L. R. Pattison, P. Petroff, M. Kawano, H. Yamada and N. Ono, *J. Appl. Phys.*, 2006, **100**, 034502.
23 S. Aramaki, Y. Sakai and N. Ono, *Appl. Phys. Lett.*, 2004, **84**, 2085–2087.
24 S. Ito, T. Murashima, N. Ono and H. Uno, *Chem. Commun.*, 1998, 1661–1662.
25 W. Zhao, D. Qian, S. Zhang, S. Li, O. Inganäs, F. Gao and J. Hou, *Adv. Mater.*, 2016, **28**, 4734–4739.
26 S. Li, L. Ye, W. Zhao, S. Zhang, S. Mukherjee, H. Ade and J. Hou, *Adv. Mater.*, 2016, **28**, 9423–9429.
27 Y. Jin, Z. Chen, S. Dong, N. Zheng, L. Ying, X.-F. Jiang, F. Liu, F. Huang and Y. Cao, *Adv. Mater.*, 2016, **28**, 9811–9818.
28 V. Vohra, K. Kawashima, T. Kakara, T. Koganezawa, I. Osaka, K. Takimiya and H. Murata, *Nat. Photonics*, 2015, **9**, 403–408.
29 B. Kan, M. Li, Q. Zhang, F. Liu, X. Wan, Y. Wang, W. Ni, G. Long, X. Yang, H. Feng, Y. Zuo, M. Zhang, F. Huang, Y. Cao, T. P. Russell and Y. Chen, *J. Am. Chem. Soc.*, 2015, **137**, 3886–3893.
30 J.-D. Chen, C. Cui, Y.-Q. Li, L. Zhou, Q.-D. Ou, C. Li, Y. Li and J.-X. Tang, *Adv. Mater.*, 2015, **27**, 1035–1041.
31 D. S. Berezin, O. V. Toldina and E. V. Kudrik, *Russ. J. Gen. Chem.*, 2003, **73**, 1309–1314.
32 M. Guide, X.-D. Dang and T.-Q. Nguyen, *Adv. Mater.*, 2011, **23**, 2313–2319.
33 N. Noguchi, S. Junwei, H. Asatani and M. Matsuoka, *Cryst. Growth Des.*, 2010, **10**, 1848–1853.
34 L. H. Hutter, B. J. Müller, K. Koren, S. M. Borisov and I. Klimant, *J. Mater. Chem. C*, 2014, **2**, 7589–7598.
35 V. Gottumukkala, O. Ongayi, D. G. Baker, L. G. Lomax and M. G. H. Vicente, *Bioorg. Med. Chem.*, 2006, **14**, 1871–1879.
36 S. Aramaki, Y. Sakai, R. Yoshiyama, K. Sugiyama, N. Ono and J. Mizuguchi, *Proc. SPIE*, 2004, **5522**, 27–35.
37 W. Shin, T. Yasuda, G. Watanabe, Y. S. Yang and C. Adachi, *Chem. Mater.*, 2013, **25**, 2549–2556.
38 38 Q. V. Hoang, C. E. Song, I.-N. Kang, S.-J. Moon, S. K. Lee, J.-C. Lee and W. S. Shin, *RSC Adv.*, 2016, **6**, 28658–28665.
39 A. Mishra, D. Popovic, A. Vogt, H. Kast, T. Leitner, K. Walzer, M. Pfeiffer, E. Mena-Osteritz and P. Bäuerle, *Adv. Mater.*, 2014, **26**, 7217–7223.
40 Y. S. Choi, T. J. Shin and W. H. Jo, *ACS Appl. Mater. Interfaces*, 2014, **6**, 20035–20042.
41 W. Ni, X. Wan, M. Li, Y. Wang and Y. Chen, *Chem. Commun.*, 2015, **51**, 4936–4950.
42 A. B. Tamayo, M. Tantiwiwat, B. Walker and T.-Q. Nguyen, *J. Phys. Chem. C*, 2008, **112**, 15543–15552.
43 K. Gao, L. Li, T. Lai, L. Xiao, Y. Huang, F. Huang, J. Peng, Y. Cao, F. Liu, T. P. Russell, R. A. J. Janssen and X. Peng, *J. Am. Chem. Soc.*, 2015, **137**, 7282–7285.
44 H. Qin, L. Li, F. Guo, S. Su, J. Peng, Y. Cao and X. Peng, *Energy Environ. Sci.*, 2014, **7**, 1397–1401.
45 H. Saeki, O. Kurimoto, H. Nakaoka, M. Misaki, D. Kuzuhara, H. Yamada, K. Ishida and Y. Ueda, *J. Mater. Chem. C*, 2014, **2**, 5357–5364.
46 T. Okujima, Y. Hashimoto, G. Jin, H. Yamada, H. Uno and N. Ono, *Tetrahedron*, 2008, **64**, 2405–2411.
47 K. Takahashi, D. Kuzuhara, N. Aratani and H. Yamada, *J. Photopolym. Sci. Technol.*, 2013, **26**, 213–216.
48 H. Yamada, K. Kushibe, T. Okujima, H. Uno and N. Ono, *Chem. Commun.*, 2006, 383–385.
49 S. Loser, C. J. Bruns, H. Miyauchi, R. P. Ortiz, A. Facchetti, S. I. Stupp and T. J. Marks, *J. Am. Chem. Soc.*, 2011, **133**, 8142–8145.
50 Y. Sato, T. Niinomi, M. Hashiguchi, Y. Matsuo and E. Nakamura, *Proc. SPIE,* 2007, **6656**, 66560U.
51 H. Tanaka, Y. Abe, Y. Matsuo, J. Kawai, I. Soga, Y. Sato and E. Nakamura, *Adv. Mater.*, 2012, **24**, 3521–3525.
52 M. Guide, J. D. A. Lin, C. M. Proctor, J. Chen, C. García-Cervera and T.-Q. Nguyen, *J. Mater. Chem. A*, 2014, **2**, 7890–7896.
53 L. Xiao, S. Chen, K. Gao, X. Peng, F. Liu, Y. Cao, W.-Y. Wong, W.-K. Wong and X. Zhu, *ACS Appl. Mater. Interfaces*, 2016, **8**, 30176–30183.
54 A. K. K. Kyaw, D. H. Wang, V. Gupta, W. L. Leong, L. Ke, G. C. Bazan and A. J. Heeger, *ACS Nano*, 2013, **7**, 4569–4577.
55 S. R. Cowan, A. Roy and A. J. Heeger, *Phys. Rev. B*, 2010, **82**, 245207.
56 A. W. Hains, Z. Liang, M. A. Woodhouse and B. A. Gregg, *Chem. Rev.*, 2010, **110**, 6689–6735.
57 B. Kippelen and J.-L. Brédas, *Energy Environ. Sci.*, 2009, **2**, 251–261.
58 O. V. Mikhnenko, P. W. M. Blom and T.-Q. Nguyen, *Energy Environ. Sci.*, 2015, **8**, 1867–1888.
59 P. Müller-Buschbaum, *Adv. Mater.*, 2014, **26**, 7692–7709.
60 I. Osaka and K. Takimiya, *Polymer*, 2015, **59**, A1–A15.
61 Q. Zhang, B. Kan, F. Liu, G. Long, X. Wan, X. Chen, Y. Zuo, W. Ni, H. Zhang, M. Li, Z. Hu, F. Huang, Y. Cao, Z. Liang, M. Zhang, T. P. Russell and Y. Chen, *Nat. Photonics*, 2015, **9**, 35–41.
62 J. A. Love, I. Nagao, Y. Huang, M. Kuik, V. Gupta, C. J. Takacs, J. E. Coughlin, L. Qi, T. S. van der Poll, E. J. Kramer, A. J. Heeger, T.-Q. Nguyen and G. C. Bazan, *J. Am. Chem. Soc.*, 2014, **136**, 3597–3606.
63 J. A. Love, C. M. Proctor, J. Liu, C. J. Takacs, A. Sharenko, T. S. van der Poll, A. J. Heeger, G. C. Bazan and T.-Q. Nguyen, *Adv. Funct. Mater.*, 2013, **23**, 5019–5026.
64 I. Osaka, T. Kakara, N. Takemura, T. Koganezawa and K. Takimiya, *J. Am. Chem. Soc.*, 2013, **135**, 8834–8837.
65 A. Sharenko, M. Kuik, M. F. Toney and T.-Q. Nguyen, *Adv. Funct. Mater.*, 2014, **24**, 3543–3550.
66 J. M. Szarko, J. Guo, Y. Liang, B. Lee, B. S. Rolczynski, J. Strzalka, T. Xu, S. Loser, T. J. Marks, L. Yu and L. X. Chen, *Adv. Mater.*, 2010, **22**, 5468–5472.
67 J. A. Reinspach, Y. Diao, G. Giri, T. Sachse, K. England, Y. Zhou, C. Tassone, B. J. Worfolk, M. Presselt, M. F. Toney, S. Mannsfeld and Z. Bao, *ACS Appl. Mater. Interfaces*, 2016, **8**, 1742–1751.
68 L. Zhao, T. Komino, M. Inoue, J.-H. Kim, J. C. Ribierre and C. Adachi, *Appl. Phys. Lett.*, 2015, **106**, 063301.
69 D. Yokoyama, A. Sakaguchi, M. Suzuki and C. Adachi, *Org. Electron.*, 2009, **10**, 127–137.